

Chronic wide-field imaging of brain hemodynamics in behaving animals

PENG MIAO,^{1,2,3} LINGKE ZHANG,¹ MIAO LI,¹ YIGUANG ZHANG,¹ SHIHAN FENG,¹ QIHONG WANG,² AND NITISH V. THAKOR^{2,4}

¹*Institute of Biomedical Engineering, School of Communication and Information Engineering, Shanghai University, Shanghai 200444, China*

²*Department of Biomedical Engineering, Johns Hopkins University, Baltimore, MD 21205, USA*

³*pengmiao@shu.edu.cn*

⁴*nitish@jhu.edu*

Abstract: Chronically monitoring cerebral activities in awake and freely moving status is very important in physiological and pathological studies. We present a novel standalone micro-imager for monitoring the cerebral blood flow (CBF) and total hemoglobin (HbT) activities in freely moving animals using the laser speckle contrast imaging (LSCI) and optical intrinsic signal (OIS) methods. A new cranial window method, using contact lens and wide field optics, is also proposed to achieve the chronic and wide-field imaging of rat's cerebral cortex. The hemodynamic activities of rats' cortex were measured for the first time without restriction of cables or fibers in awake and behaving animals. Chronic imaging showed the increase of CBF and HbT in motor cortex when the rats were climbing on the cage wall. Interestingly, the CBF activation of supplying vessel was smaller than that of parenchyma. Furthermore, after the climbing, CBF demonstrated fully return to the baseline while HbT showed a delayed recovery. The standalone micro-imager technology provides new possibilities of brain imaging in cognitive neuroscience studies.

© 2016 Optical Society of America

OCIS codes: (170.2655) Functional monitoring and imaging; (170.3880) Medical and biological imaging; (110.6150) Speckle imaging; (170.5380) Physiology; (170.0110) Imaging systems.

References and links

1. J. N. D. Kerr and W. Denk, "Imaging in vivo: watching the brain in action," *Nat. Rev. Neurosci.* **9**(3), 195–205 (2008).
2. K. M. Tye and K. Deisseroth, "Optogenetic investigation of neural circuits underlying brain disease in animal models," *Nat. Rev. Neurosci.* **13**(4), 251–266 (2012).
3. J. W. Lichtman and W. Denk, "The big and the small: challenges of imaging the brain's circuits," *Science* **334**(6056), 618–623 (2011).
4. C. M. Niell and M. P. Stryker, "Modulation of visual responses by behavioral state in mouse visual cortex," *Neuron* **65**(4), 472–479 (2010).
5. T. A. Szuts, V. Fadeyev, S. Kachiguine, A. Sher, M. V. Grivich, M. Aggrochão, P. Hottowy, W. Dabrowski, E. V. Lubenov, A. G. Siapas, N. Uchida, A. M. Litke, and M. Meister, "A wireless multi-channel neural amplifier for freely moving animals," *Nat. Neurosci.* **14**(2), 263–269 (2011).
6. A. K. Lee, I. D. Manns, B. Sakmann, and M. Brecht, "Whole-cell recordings in freely moving rats," *Neuron* **51**(4), 399–407 (2006).
7. D. A. Dombeck, A. N. Khabbaz, F. Collman, T. L. Adelman, and D. W. Tank, "Imaging large-scale neural activity with cellular resolution in awake, mobile mice," *Neuron* **56**(1), 43–57 (2007).
8. J. Sawinski, D. J. Wallace, D. S. Greenberg, S. Grossmann, W. Denk, and J. N. D. Kerr, "Visually evoked activity in cortical cells imaged in freely moving animals," *Proc. Natl. Acad. Sci. U.S.A.* **106**(46), 19557–19562 (2009).
9. F. Helmchen, M. S. Fee, D. W. Tank, and W. Denk, "A miniature head-mounted two-photon microscope. high-resolution brain imaging in freely moving animals," *Neuron* **31**(6), 903–912 (2001).
10. B. A. Flusberg, A. Nimmerjahn, E. D. Cocker, E. A. Mukamel, R. P. J. Barretto, T. H. Ko, L. D. Burns, J. C. Jung, and M. J. Schnitzer, "High-speed, miniaturized fluorescence microscopy in freely moving mice," *Nat. Methods* **5**(11), 935–938 (2008).
11. K. Murari, R. Etienne-Cummings, G. Cauwenberghs, and N. Thakor, "An integrated imaging microscope for untethered cortical imaging in freely-moving animals," in *Proceedings of 2010 Annual International Conference of the IEEE Engineering in Medicine and Biology (EMBC, 2010)*, pp. 5795–5798.

12. K. K. Ghosh, L. D. Burns, E. D. Cocker, A. Nimmerjahn, Y. Ziv, A. E. Gamal, and M. J. Schnitzer, "Miniaturized integration of a fluorescence microscope," *Nat. Methods* **8**(10), 871–878 (2011).
13. P. Miao, H. Lu, Q. Liu, Y. Li, and S. Tong, "Laser speckle contrast imaging of cerebral blood flow in freely moving animals," *J. Biomed. Opt.* **16**(9), 090502 (2011).
14. R. Liu, Q. Huang, B. Li, C. Yin, C. Jiang, J. Wang, J. Lu, Q. Luo, and P. Li, "Extendable, miniaturized multi-modal optical imaging system: cortical hemodynamic observation in freely moving animals," *Opt. Express* **21**(2), 1911–1924 (2013).
15. A. Grinvald, E. Lieke, R. D. Frostig, C. D. Gilbert, and T. N. Wiesel, "Functional architecture of cortex revealed by optical imaging of intrinsic signals," *Nature* **324**(6095), 361–364 (1986).
16. E. Shtoyerman, A. Arieli, H. Slovlin, I. Vanzetta, and A. Grinvald, "Long-term optical imaging and spectroscopy reveal mechanisms underlying the intrinsic signal and stability of cortical maps in V1 of behaving monkeys," *J. Neurosci.* **20**(21), 8111–8121 (2000).
17. I. Sigal, M. M. Koletar, D. Ringuette, R. Gad, M. Jeffrey, P. L. Carlen, B. Stefanovic, and O. Levi, "Imaging brain activity during seizures in freely behaving rats using a miniature multi-modal imaging system," *Biomed. Opt. Express* **7**(9), 3596–3609 (2016).
18. A. Y. Shih, J. D. Driscoll, P. J. Drew, N. Nishimura, C. B. Schaffer, and D. Kleinfeld, "Two-photon microscopy as a tool to study blood flow and neurovascular coupling in the rodent brain," *J. Cereb. Blood Flow Metab.* **32**(7), 1277–1309 (2012).
19. P. J. Drew, A. Y. Shih, J. D. Driscoll, P. M. Knutsen, P. Blinder, D. Davalos, K. Akassoglou, P. S. Tsai, and D. Kleinfeld, "Chronic optical access through a polished and reinforced thinned skull," *Nat. Methods* **7**(12), 981–984 (2010).
20. A. Holtmaat, T. Bonhoeffer, D. K. Chow, J. Chuckowree, V. De Paola, S. B. Hofer, M. Hübener, T. Keck, G. Knott, W. C. A. Lee, R. Mostany, T. D. Mrsic-Flogel, E. Nedivi, C. Portera-Cailliau, K. Svoboda, J. T. Trachtenberg, and L. Wilbrecht, "Long-term, high-resolution imaging in the mouse neocortex through a chronic cranial window," *Nat. Protoc.* **4**(8), 1128–1144 (2009).
21. J. Wang, Y. Wang, B. Li, D. Feng, J. Lu, Q. Luo, and P. Li, "Dual-wavelength laser speckle imaging to simultaneously access blood flow, blood volume, and oxygenation using a color CCD camera," *Opt. Lett.* **38**(18), 3690–3692 (2013).
22. N. Pouratian, A. F. Cannestra, N. A. Martin, and A. W. Toga, "Intraoperative optical intrinsic signal imaging: a clinical tool for functional brain mapping," *Neurosurg. Focus* **13**(4), e1 (2002).
23. A. K. Dunn, A. Devor, H. Bolay, M. L. Andermann, M. A. Moskowitz, A. M. Dale, and D. A. Boas, "Simultaneous imaging of total cerebral hemoglobin concentration, oxygenation, and blood flow during functional activation," *Opt. Lett.* **28**(1), 28–30 (2003).
24. A. K. Dunn, H. Bolay, M. A. Moskowitz, and D. A. Boas, "Dynamic imaging of cerebral blood flow using laser speckle," *J. Cereb. Blood Flow Metab.* **21**(3), 195–201 (2001).
25. D. A. Boas and A. K. Dunn, "Laser speckle contrast imaging in biomedical optics," *J. Biomed. Opt.* **15**(1), 011109 (2010).
26. P. Miao, A. Rege, N. Li, N. V. Thakor, and S. Tong, "High resolution cerebral blood flow imaging by registered laser speckle contrast analysis," *IEEE Trans. Biomed. Eng.* **57**(5), 1152–1157 (2010).
27. A. Rege, J. Senarathna, N. Li, and N. V. Thakor, "Anisotropic processing of laser speckle images improves spatiotemporal resolution," *IEEE Trans. Biomed. Eng.* **59**(5), 1272–1280 (2012).
28. O. Yang and B. Choi, "Laser speckle imaging using a consumer-grade color camera," *Opt. Lett.* **37**(19), 3957–3959 (2012).
29. A. B. Parthasarathy, W. J. Tom, A. Gopal, X. Zhang, and A. K. Dunn, "Robust flow measurement with multi-exposure speckle imaging," *Opt. Express* **16**(3), 1975–1989 (2008).
30. A. Rege, K. Murari, A. Seifert, A. P. Pathak, and N. V. Thakor, "Multiexposure laser speckle contrast imaging of the angiogenic microenvironment," *J. Biomed. Opt.* **16**(5), 056006 (2011).

1. Introduction

Monitoring brain activity during active and social behavioral conditions provides more relevant physiological information and realistic information on pathological conditions [1–3]. The methods and tools for measuring neurophysiological activity in awake, behaving animals including electrophysiological methods (such as EEG [4], LFP/Spike [5], whole-cell recording [6]) and imaging methods (such as two-photon [7–9], fluorescence imaging [10–12], laser speckle contrast imaging (LSCI) [13,14], and optical intrinsic signal imaging (OIS) [15,16]. While the electrophysiological methods provide an instantaneous recording of neural activities in the brain, optical imaging methods probe the brain's hemodynamics in a non-contact way and provide structural and functional information at high resolution.

For freely moving animals, miniaturized optical imaging systems have been developed but the usage of fibers (light delivery [13] or image transmission [14]) and cables (data transmission and power supply [17]) limits the mobility of the subjects. Furthermore,

traditional imaging system cannot be applied to investigate the brain activities in social behavior and social motivations of groups.

Chronic imaging of the brain functions is also important, for example, to demonstrate the cognitive activities in nonhuman primate brain [16] and to measure the cerebral blood flow (CBF) and metabolism changes after seizures in rats [17]. Traditional methods for chronic imaging require a cranial window for a high-quality optical access [17,18]. Recently proposed thinned-skull technique has gained acceptance as a less invasive procedure [19]. However, it is usually difficult to make the thinned-skull window larger than $10 \times 10 \text{ mm}^2$ for wide-field imaging. The cranial window technique involves a full craniotomy with a cover glass filled with agarose [20]. Due to inflammation or physiological changes, the cover glass may apply additional pressure disrupting cerebrospinal fluid regulation and intracranial pressure levels [19]. Furthermore, the cover glass is rigid so that it cannot be used for covering lateral areas of rat's cortex.

In this study, for the first time, we developed a new standalone micro-imager without fiber and cable connections. Our approach, based on compact design and micro-optics achieves greater miniaturization and provides better feasibility in monitoring CBF and total hemoglobin (HbT) activities in behaving animals. A new contact lens based cranial window method is also proposed to achieve wide-field chronic imaging of rat's cortex. As a demonstrative application, the hemodynamic responses of rats' motor cortex during climbing on the cage wall were measured and analyzed. The combination of micro-imager and optical cranial window in our design yields opportunities of chronic brain hemodynamic monitoring in behaving animals.

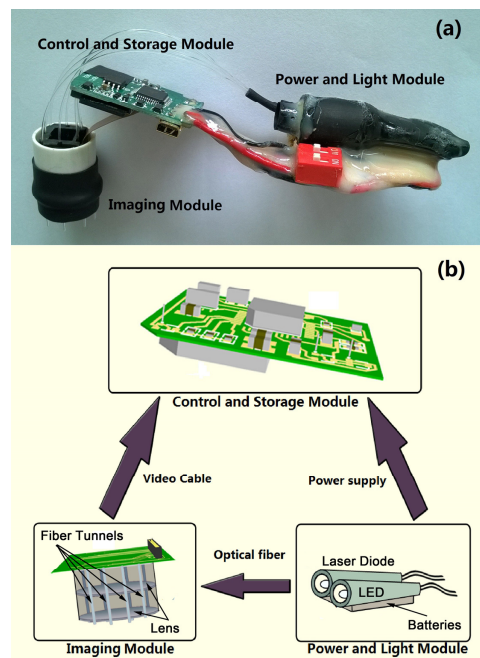


Fig. 1. The proposed standard alone micro-imager (a) and its design diagram (b): (i) Imaging Module (IM), (ii) Control and Storage Module (CSM), (iii) Powering and Light Module (PLM).

2. Standalone micro-imager

The standalone micro-imager (Fig. 1(a)) consists of (i) Imaging Module (IM), (ii) Control and Storage Module (CSM), (iii) Power and Light Module (PLM). The IM (the weight of 1.5g, the width of 10mm, and the height of 16mm) employs an anti-reflection coating achromatic

doublets lens (Thorlabs, Inc.) and a 1/4 inch CMOS sensor (OV5640, OmniVision, Inc.) to collect reflected light from brain cortex. To facilitate the mounting of IM, a plastic cylinder base was permanently attached to the cranium with dental cement. A fixing screw is used to adjust the imaging focus. The CMOS sensor outputs 30 raw images $I_{\text{raw}}(x, y)$ each second with a spatial resolution of 1920 x 1080 pixels. A 2×2 hardware binning and 10-bit RAW RGB mode was used in this study. The sensitivity of the color sensor is 600 mV/lux-sec with dynamic range of 68 dB (8x gain). The CMOS sensor utilizes the Bayer color filter array to separate different color information in the raw image and the 'R', 'G', 'B' channels can be reconstructed as $I_R(x, y)$, $I_G(x, y)$ and $I_B(x, y)$ [21].

To minimize the weight on animal's head, IM part was separated from the CSM through FPC (Flexible Printed Circuit) connections. The CSM gets the imaging readout from the CMOS sensor and automatically stores the raw image in the mini SD card. There is a mini-USB interface within the CSM for on-line communication between the computer and the controlling MCU. We use this interface to download programs and monitor in real-time while mounting the IM.

The light sources are the 635 nm laser diode (HL6322G, 15 mW, Hitachi, Ltd.) and the single color LED (LXZ1-PX01, 566 nm ~569 nm, 300 mW, LUMILEDS). The light was delivered through a multi-mode fiber bundle (8 fibers, 4 for laser light and 4 for LED light, 12 μm core, 0.45 NA; SMOIF, Shanghai, China). The front ends of the fiber bundle were fixed in the narrow tunnels positioned uniformly around the outside of micro-lens, providing uniform illumination (IM in Fig. 1(b)). Because of the specific wavelength of both light sources, the reflectance images from the LED and laser light are separately collected in the 'G' channel $I_G(x, y)$ and the 'R' channel $I_R(x, y)$ in the recorded images.

Two lithium batteries (3V, 1500mAh) supply the power and allows 30-minute continuous recording. There is also a switch button to turn the imager on and off manually. The CSM and PLM are placed together on the animal's backpack to facilitate the freely moving applications (Fig. 2(b); corresponding movie is shown in [Visualization 1](#)).

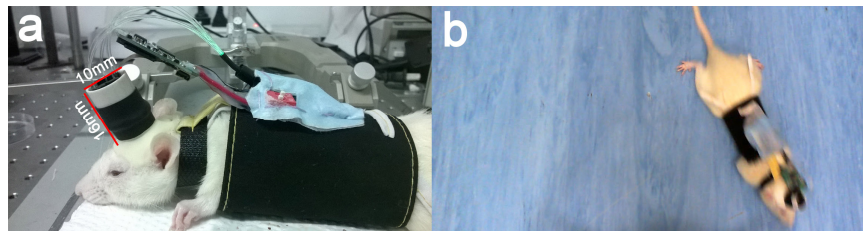


Fig. 2. The stand-alone micro-imager is wearable (a) and feasible for imaging rat's brain activities when freely moving in the open field (b). Also, see the supplementary video ([Visualization 1](#)).

3. Cranial window

To make a wide-field cranial window on rat's cerebral cortex, a new preparation method was developed based on contact lens. The surgery was performed in our Specific Pathogen-Free (SPF) Animal Research Facility (ARF). Before the surgery, the rats were anesthetized with an intraperitoneal injection of ketamine (80 mg/kg) and xylazine (5 mg/g) mixture. The rats were then placed on a heating blanket and the head was stabilized in a stereotaxic frame. During the surgical procedure, the eyes were protected from dehydration and irritation by applying Vaseline.

A flap of skin covering the head skull was removed using scissors. Then, 1% Xylocaine was applied to the periosteum of the skull and its exposed muscles. After removal of the periosteum, the cortical area of interest (a 10x15 mm² area was centered at the right cerebral hemisphere and covers the somatosensory and motor cortex areas) was thinned gently and

saline was applied to avoid heating. When the cortical surface vasculature in the thinned area was visible, the angle-tipped forceps was used to lift the thinned bone and expose the dura. Gelfoam (soaked in the cortex buffer) was applied to stop bleeding in the dura and make the area clear. Then, a thin layer of melted 1.2% agarose was applied to cover the exposed dura before we made the cranial window.

As a flexible and biocompatible material, the contact lens was used as the main interface of craniotomy in this study. The contact lens can be easily clipped to fit the exposed dura. Dental cement was used to seal the side of the optical window to the skull. After surgical manipulation, the rats were allowed to recover for 5 days in a high-ceiling cage with free access to food and water. During the recovery, infections were controlled with a daily intraperitoneal injection of Carprofen (5 mg/kg). Under standard conditions in the SPF ARF, the cranial window can provide optically transparent access to the imaging area up to 3 weeks after the surgery (Fig. 3).

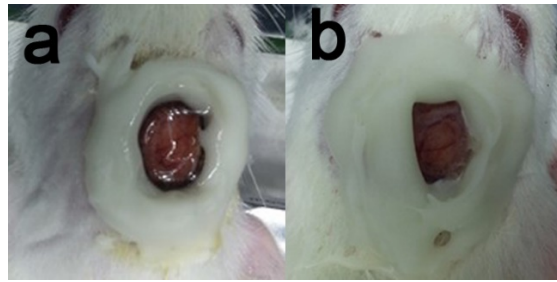


Fig. 3. The cranial window preparation for chronic wide-field imaging using contact lens: (a) cranial window on day 0; (b) cranial window after three weeks.

4. Data processing

4.1 Optical intrinsic signal (OIS) imaging

Under the LED illumination (566 nm ~569 nm), both oxy- and deoxy- hemoglobin have equal absorption coefficients [22]. Therefore, the changes of 'G' channel images reflect the activities of total hemoglobin concentration. To improve the SNR, all $I_G(x, y)$ s were registered (See 4.3) and then every five consecutive 'G' channel images were averaged to obtain one OIS image $I_{OIS}(x, y)$. For pixel (x, y) at time point t , OIS signal $I_{OIS}(x, y, t)$ can be used to estimate the relative changes of total hemoglobin concentration, *i.e.* $rHbT$, according to the Lambert-Beer law [23]:

$$rHbT(x, y, t) = (1/\varepsilon D) \ln [I_{OIS}(x, y, 0) / I_{OIS}(x, y, t)] \quad (1)$$

In Eq. (1), ε is the molar extinction coefficients, D is the differential path length factor. Figure 4(a) showed a typical OIS image obtained in this study.

4.2 Laser speckle contrast imaging (LSCI)

For each $I_R(x, y)$, a 7×7 spatial window is applied to produce the corresponding contrast images $K_s^2(x, y, i)$ based on Eq. (2) [24].

$$K_s = \frac{\sigma_s}{\langle I \rangle} \quad (2)$$

where σ_s and $\langle I \rangle$ are the spatial standard deviation and spatial average of the speckle intensities.

The relation between K_s and blood flow speed v is described by Eq. (3) and Eq. (4) [25].

$$K_s^2 = \beta \left\{ \frac{\tau_c}{T} + \frac{\tau_c^2}{2T^2} [\exp(-\frac{2T}{\tau_c}) - 1] \right\} \quad (3)$$

$$\tau_c \propto 1/v \quad (4)$$

where τ_c is the correlation time, T is the exposure time, and β is a parameter related to detector size, speckle size, and polarization.

Before the contrast calculation, all speckle images were registered to eliminate the effects of motion artifacts [26]. Then, the contrast images were calculated and five successive contrast images were averaged to improve the imaging SNR [27]. Figure 4(b) shows a typically averaged contrast image $K_s^2(x, y)$ obtained using the micro-imager.

To compare the CBF activities in behavior status, the relative changes of CBF within the region of interest (ROIs), defined as $rCBF$, were calculated based on Eq. (5):

$$rCBF = \frac{v(t)}{v(0)} = \frac{\tau_c(0)}{\tau_c(t)} \quad (5)$$

4.3 Registration of both LSCI and OIS images

The motion artifacts contribute the major noise in the data recorded from behavior animals. In this study, registration based work flow is applied in processing of both LSCI and OIS images [13]. Registration is started with the “R” channel speckle images $I_R(x, y, t)$ which are aligned to the first frame $I_R(x, y, 0)$ by registered laser speckle contrast analysis (rLASCA) method [26]. Basically, rLASCA processes the speckle image with a 3×3 convolution kernel, and then registered by normalized correlation metric and finally resampled with cubic B-spline interpolator. After the registration, contrast images are calculated using Eq. (2). Then, same registration parameters are used for registration of corresponding “G” channel images $I_G(x, y, t)$.

5. Experiments

The experimental protocol used in this study was approved by the Institutional Animal Care and Use Committee of Shanghai University (No.20150306021). All experiments were performed in our SPF ARF. Five rats (250g~300g) were involved in this study. Before the micro-imager installation, the rats were anesthetized using 5% isoflurane. Then, the backpack containing the CSM and PLM was dressed onto the rat's body. Afterward, the IM was installed onto the cylinder base and FPC connections were set up for imaging control and data transmission. The micro-imager was then connected to a computer for on-line focus adjustment.

The imaging experiments were performed when the rats ($n = 5$) were freely moving in the open field (Fig. 2(b)) and in the cage (also see the supplementary video [Visualization 1](#)). At the same time, a video camera recorded animals' behaviors. During the experiments in the cage, the rats were occasionally climbing on the cage wall. These “climbing sessions” were identified and the corresponding data were extracted and further segmented into three subsections: before climbing, climbing on the wall (rearing up), after climbing. Statistical analysis of $rCBF$ and $rHbT$ in three subsections was performed on a total of 20 climbing sessions (4 climbing sessions each rat). To validate the stability of chronic imaging, all imaging experiments were performed on Day 0 and Day 20.

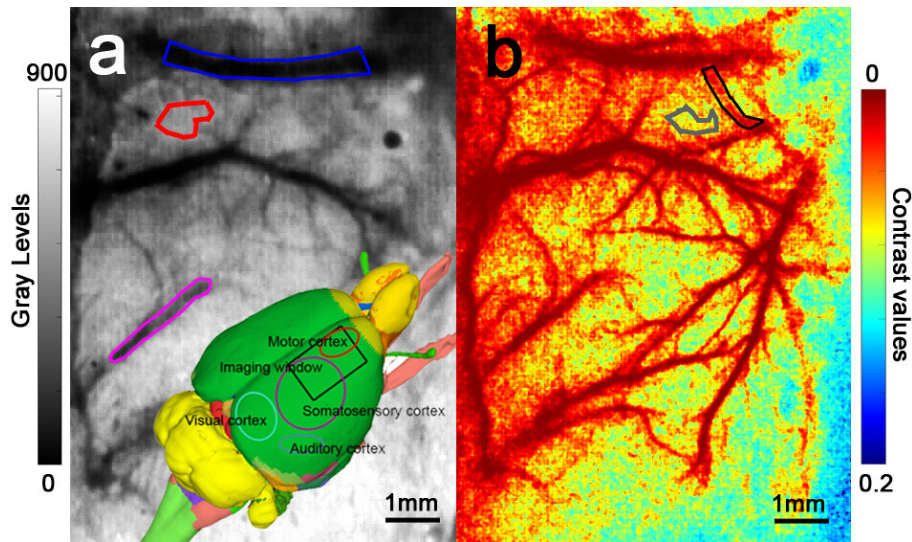


Fig. 4. Wide-field imaging of brain activities in freely moving status: (a) the OIS image, (b) the contrast image. In (a), the inserted brain phantom shows the imaging window (black box). Two vessels (marked in blue and magenta) and parenchyma area (marked in red) are selected for further analysis. In (b), the supplying artery (marked in black) of the motor cortex and surrounding parenchyma area (marked in gray) are selected as ROIs. Gray bar represents the gray levels in (a), and the color bar represents the contrast values in (b).

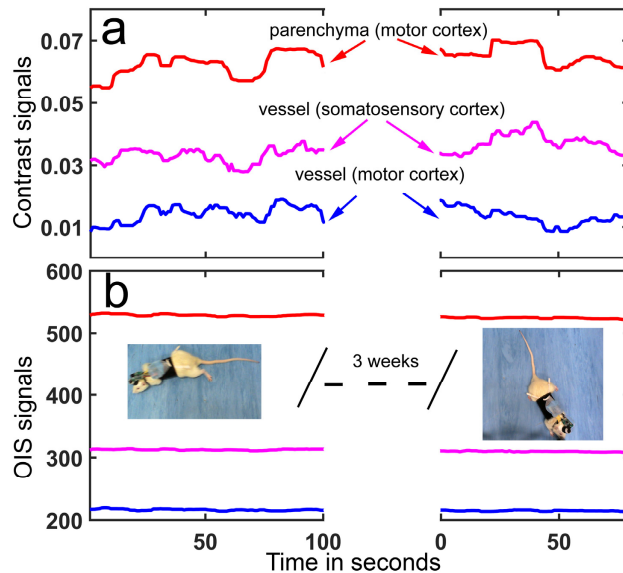


Fig. 5. Chronic monitoring the contrast signals (a) and OIS signals (b) at the selected ROIs (marked in Fig. 4(a)) when the rats were freely moving in the open-field.

6. Results

6.1 Chronically monitoring the rats' brain activities when freely moving in the open-field

To observe the rats' brain activities in freely moving status, both somatosensory and motor cortex areas were imaged using the micro-imager. Figure 4(a) and 4(b) show the OIS image $I_{OIS}(x, y)$ and contrast image $K_s^2(x, y)$ obtained in one recording experiment. In the OIS

image, the reflective intensities, *i.e.* gray levels, are modulated by the total hemoglobin concentration: larger HbT concentration results in higher absorptions of the LED light, and thus smaller gray levels (Fig. 4(a)). For the LSCI, contrast image demonstrated the CBF distribution where blood vessel areas have smaller contrast values compared to that of parenchyma area (Fig. 4(b)).

In the open-field freely moving experiment, the vessels and parenchyma covering motor and somatosensory cortex areas were selected as ROIs (marked in blue, red and magenta colors in Fig. 4(a)). Figure 5(a) shows the recorded contrast signals and Fig. 5(b) presents the corresponding OIS signals. Different ROIs show different baseline levels during the imaging due to different status of metabolism. All signals recorded after three weeks maintained consistent and stable levels. This result confirmed the reliability of standalone micro-imager in chronic imaging. Compared with the OIS signals, however, contrast values demonstrate more variations in the freely moving experiments.

6.2 Changes of rCBF and rHbT when the rats were climbing on the cage wall

On day 0, a total of 20 climbing sessions were identified when the rats ($n = 5$) were freely moving in the cage. Since these climbing events happened occasionally, they usually had different time course. Figure 6(a) and 6(b) show the time course of one climbing session. Therefore, the accurate alignment of all 20 events cannot be achieved. Furthermore, the transitions from standing to rearing up (and reverse) also varied in different sessions. Therefore, to make the statistical analysis more reliable, data in transition procedure were excluded and the average of 3-second signal in each subsection was applied (see the subsections marked in Fig. 6(a)).

Cortical branches of middle cerebral artery (MCA) supplying motor cortex and its surrounding parenchyma area were selected as ROIs (marked in Fig. 4(b)). Statistical analysis of all 20 sessions are presented in the bar graph in Fig. 6(c) and 6(d). In Fig. 6(a), compared with the vessel area, rCBF in the parenchyma area demonstrates a statistically significant difference during the rearing up status ($p < 0.01$, Fig. 6(c)). However, the relative changes of rHbT in these two areas do not show significant differences (Fig. 6(b) and 6(d)).

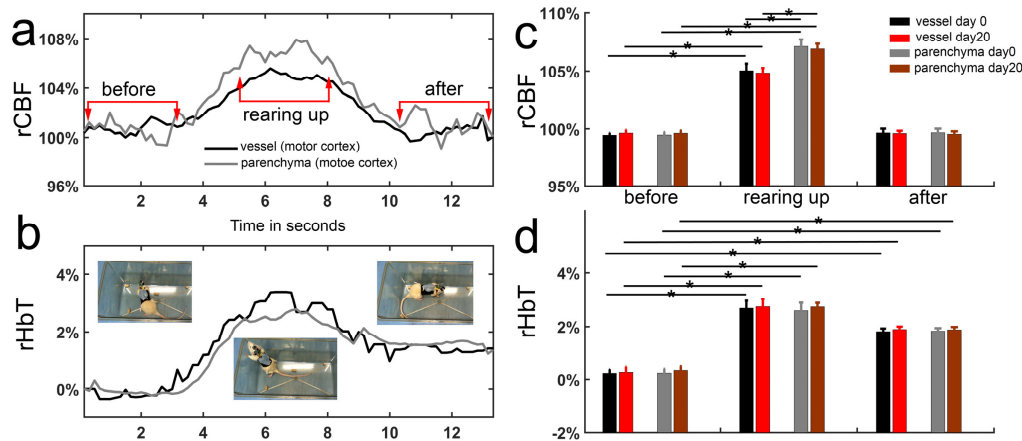


Fig. 6. Changes of rCBF and rHbT when the rats were climbing on the wall. (a) and (b) shows the rCBF and rHbT activities of the ROIs (marked in Fig. 4(b)) in one climbing session. (c) and (d) demonstrate the statistical analysis of the rCBF and rHbT in all 20 climbing sessions on day 0 and day 20 (* indicates a significant difference with $p < 0.01$).

In Fig. 6(c), compared to the baseline (before climbing), rCBFs in vessel and parenchyma demonstrate an up-regulation during the rearing up ($105.03\% \pm 0.61\%$ on day 0 and $104.83\% \pm 0.43\%$ on day 20, $p < 0.01$) and a fast and full recovery after the climbing ($99.66\% \pm 0.36\%$ on day 0 and $99.60\% \pm 0.23\%$ on day 20, $p > 0.05$). For the rHbTs in Fig. 6(d), there are also

activation in the rearing up status ($2.68\% \pm 0.28\%$ on day 0 and $2.74\% \pm 0.28\%$ on day 20, $p < 0.01$). But, the recoveries of HbT are delayed ($1.81\% \pm 0.11\%$ on day 0 and $1.89\% \pm 0.12\%$ on day 20, $p < 0.01$) compared to the baseline.

Furthermore, the statistical analysis shows no significant differences between the data acquired on day 0 and on day 20. The consistent results again demonstrate the stability of cranial window and feasibility of new micro-imager for chronic imaging applications.

7. Discussions

7.1 Freely moving feasibility

In the movie (shown in [Visualization 1](#)), rats wearing the micro-imager behaved in a truly free moving status, like rubbing face, eating, running, tracking, and climbing. The feasibility comes from the small size ($16\text{mm} \times 10\text{mm}$) and weight (1.5g) of the IM. The standalone aspect also releases the requirement of fibers and cables in previously published solutions [13, 17]. This makes the standalone micro-imager as a new brain imaging tool for cognitive neuroscience, like applications in the maze experiments, or the study of social behavior and social motivation in groups.

In the current version, the storage and battery capacity limit the continuous imaging less than 30 mins. Adding more batteries may extend the imaging time but will also increase the backpack weight and limit the animal's mobility. Using new kinds of light source, like Vertical Cavity Surface Emitting Lasers (VCSELs), may provide better solution because it will significantly reduce the power demand.

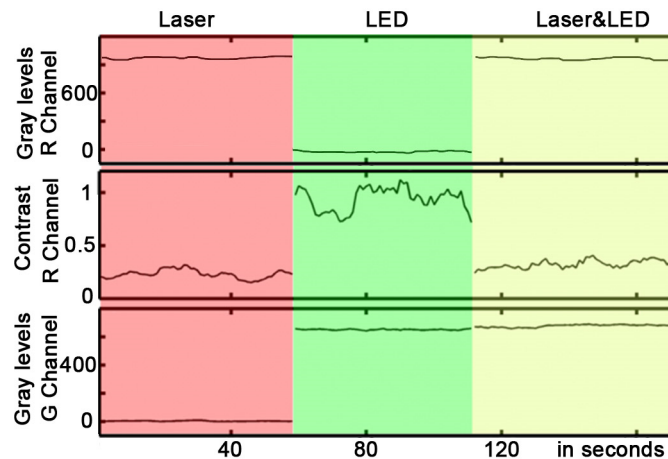


Fig. 7. The signal crosstalk of the micro-imager in simultaneous LSCI and OIS imaging.

7.2 Signal crosstalk in LSCI and OIS imaging

In this study, the laser light and LED light illuminate the rat's brain simultaneously. The Bayer color filter array in the CMOS sensor separates the reflectance light into "R" and "G" channels [21, 28]. The signal crosstalk may still exist and affect the accuracy of LSCI and OIS imaging.

We tested the signal crosstalk by continuously imaging the rat's intact skull under laser (alone), LED (alone), and both light illuminations. The rat's intact skull provides a static object without the effects of perfusion changes. In Fig. 7, the "R" channel outputs stable gray levels and contrast signals under laser (alone) and both light illuminations. While the "G" channel outputs stable OIS signals under LED (alone) and both light illuminations. These results confirmed that the signal crosstalk between LSCI and OIS imaging is minimal.

It is interesting that "R" channel outputs unstable contrast values around 1 when the only LED illuminates the imaging area. We noticed that the intensity values of "R" channel are

close to zero under LED illumination; therefore both the numerator and denominator in Eq. (1) are close to zero. This is what makes the contrast signals unstable.

7.3 Multi-exposure LSCI and thinned skull preparation

In this study, contact lens method improves the cranial window preparation for wide-field imaging. However, it provides stable and transparent cranial window for only up to 3 weeks due to the growth or regeneration of the dura and skull. Therefore, if small imaging area is needed, then the traditional cranial window or thinned skull preparation should be considered for imaging access longer than 3 weeks. Thinned skull preparation also has benefits like simpler surgical preparation and better control of intracranial pressure. For the thinned skull preparation, the standalone micro-imager can be updated with the multi-exposure strategy [29, 30] for a robust CBF measurement.

7.4 Further extension of the standalone micro-imager to resolve the details of metabolism

The current micro-imager system using color CMOS sensor where the “R” and “G” channels are already recruited for blood flow and total hemoglobin measurement. It has demonstrated good sensitivity for monitoring brain activities in behavioral animals. In some applications, detail information of metabolism, like oxy- and deoxy- hemoglobin, is needed to obtain a fully understanding of the brain’s function in pathophysiological conditions, *e.g.* stroke or seizures. The distribution of oxy- and deoxy- hemoglobin can also distinguish of arterial and venous vessels.

Although integrating a blue light source in PLM provides one options for the metabolism measurement, the power demand and penetration depth limitations make it undesirable. Adding another light source working in “R” channel provides better solution to measure metabolism [17]. To achieve this option, the running software of CSM should be updated with precise control of exposure and light switch.

8. Conclusions

Chronic monitoring of brain activity and particularly its metabolism, in behaving status, is important in physiological and pathological studies of brain functions. In this study, we developed a new standalone micro-imager with novel contact lens preparation for chronically monitoring the rat’s cortical CBF and HbT activities. The standalone micro-imager technique shows potentials for behavioral and cognitive neuroscience studies like investigation of brain activities in social behavior and social motivations.

Funding

National Natural Science Foundation of China (NSFC) (61201057, 61571284); NIH (R01HL071568). P. Miao was also supported by Chen Guang Project and China Scholarship Council (CSC).

Acknowledgments

The authors want to thank Yang Li, Zhe Yu and Zhaocheng Su for the assistant in the experimental data recording.